Cell Reports
Physical Science

CellPress
OPEN ACCESS

Article

Unveiling the Active Site of Metal-Free Nitrogen-doped Carbon for Electrocatalytic Carbon Dioxide Reduction

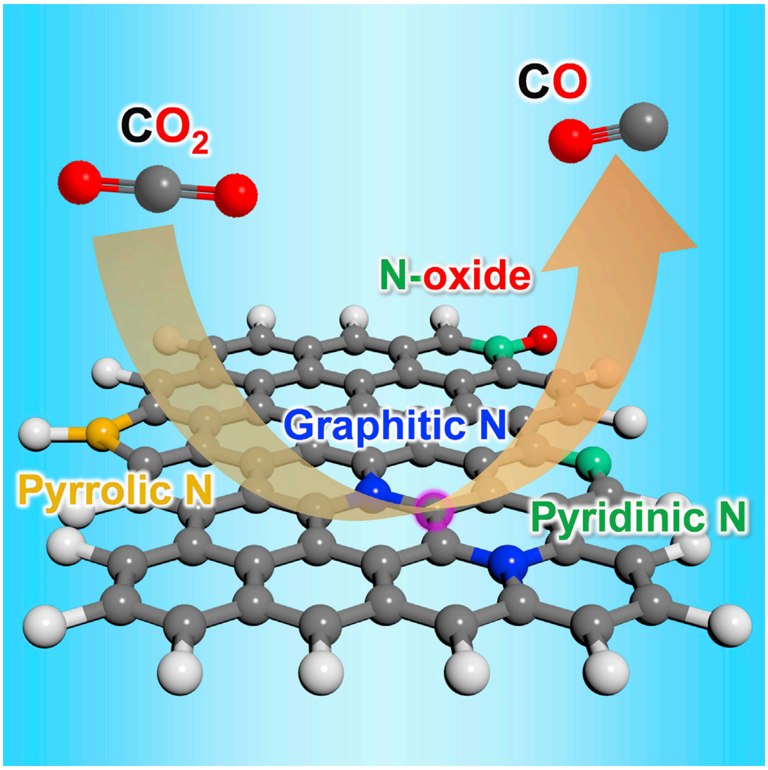

The nature of the active sites for electrocatalytic CO_2 reduction to CO on metal-free nitrogen-doped carbon remains under debate. Here, by precisely tuning the types of nitrogen dopants, Zhang et al. elucidate that graphitic nitrogen triggers CO_2 reduction, while pyridinic nitrogen promotes hydrogen evolution and pyrrolic nitrogen disfavors both reactions.

Zheng Zhang, Liang Yu, Yunchuan Tu, Ruixue Chen, Lihui Wu, Junfa Zhu, Dehui Deng

dhdeng@dicp.ac.cn

HIGHLIGHTS

Controllable tuning of nitrogen types in nitrogen-doped carbon foams

Graphitic nitrogen triggers electrocatalytic CO_2 reduction on adjacent carbon atoms

Pyridinic nitrogen favors hydrogen evolution reaction at edge carbon sites

Pyrrolic nitrogen disfavors both the CO_2 reduction and hydrogen evolution reactions

Zhang et al., Cell Reports Physical Science *1*, 100145
August 26, 2020 © 2020 The Authors.
https://doi.org/10.1016/j.xcrp.2020.100145

Please cite this article in press as: Zhang et al., Unveiling the Active Site of Metal-Free Nitrogen-doped Carbon for Electrocatalytic Carbon Dioxide Reduction, Cell Reports Physical Science (2020), https://doi.org/10.1016/j.xcrp.2020.100145

Cell Reports
Physical Science

CellPress
OPEN ACCESS

Article

Unveiling the Active Site of Metal-Free Nitrogen-doped Carbon for Electrocatalytic Carbon Dioxide Reduction

Zheng Zhang,[1,2,4] Liang Yu,[2,4] Yunchuan Tu,[1,2] Ruixue Chen,[1,2] Lihui Wu,[3] Junfa Zhu,[3] and Dehui Deng[1,2,5,*]

SUMMARY

Nitrogen-doped (N-doped) carbon materials have been widely studied for electrocatalytic CO_2R to CO. However, the active sites in N-doped carbon remain under debate owing to the complication in N types and the challenge in controllable synthesis. Here, via an innovative approach of template-assisted pyrolysis of phthalocyanine, we achieve a controlled preparation of N types in N-doped carbon foams. Electrochemical experiments show that the catalyst dominated by graphitic N rather than other N types drives highly selective CO_2R to CO against the hydrogen evolution reaction, which achieves a CO Faradaic efficiency of 95% at −0.5 V versus RHE and runs stably for 80 h. Theoretical calculations indicate that carbon atoms next to graphitic N are triggered for the CO production, while carbon atoms next to pyridinic N promote the hydrogen evolution and pyrrolic N disfavors both reactions.

INTRODUCTION

Electrocatalytic CO_2R to CO provides a potential process for converting greenhouse gases to valuable chemicals via the important chemical feedstock CO.[1–7] Previous studies indicated that nitrogen-doped (N-doped) carbon (C) materials exhibit high catalytic performance for the reaction owing to the modulated activity by N-doping.[8–12] The N dopants in the C lattice mainly exist in four doping types, including graphitic N (GN), pyridinic N (PN), pyrrolic N (ProN), and N-oxide ($N\text{-}O_x$), which have distinct structural and electronic properties.[13–16] Recently, much effort has been devoted to unveiling the origin of activity from N-doping for the electrocatalytic CO_2R to CO.[17–20] Both graphitic and pyridinic N have been reported as being capable of triggering catalytic activity for the reaction.[19,20] However, owing to the complicacy in different types of N dopants inducing the activity, the active centers for the CO_2R to CO over the N-doped carbon (NC) materials are still under debate. Identifying the N dopants that promote the catalytic activity is critical for rationally designing high-performance catalysts for this reaction and yet challenging, owing to the hardness in the controllable synthesis of NC with targeted N type.

In this work, on the basis of a template-assisted pyrolysis method, a series of NC foams with controllable N types (GN, PN, ProN, and $N\text{-}O_x$) and contents have been synthesized. The catalyst with only GN dopants exhibits the optimum activity, with a Faradaic efficiency (FE) of 95% for CO_2R to CO at a mild potential of −0.5 V versus reversible hydrogen electrode (RHE), in contrast to those with a relatively lower content of GN and higher contents of PN, ProN, or $N\text{-}O_x$. The excellent activity

---

[1] State Key Laboratory of Physical Chemistry of Solid Surfaces, Collaborative Innovation Center of Chemistry for Energy Materials (iChEM), College of Chemistry and Chemical Engineering, Xiamen University, Xiamen 361005, China

[2] State Key Laboratory of Catalysis, iChEM, Dalian Institute of Chemical Physics, Chinese Academy of Sciences, Dalian 116023, China

[3] National Synchrotron Radiation Laboratory, University of Science and Technology of China, Hefei 230029, China

[4] These authors contributed equally

[5] Lead Contact

*Correspondence: dhdeng@dicp.ac.cn

https://doi.org/10.1016/j.xcrp.2020.100145

Please cite this article in press as: Zhang et al., Unveiling the Active Site of Metal-Free Nitrogen-doped Carbon for Electrocatalytic Carbon Dioxide Reduction, Cell Reports Physical Science (2020), https://doi.org/10.1016/j.xcrp.2020.100145

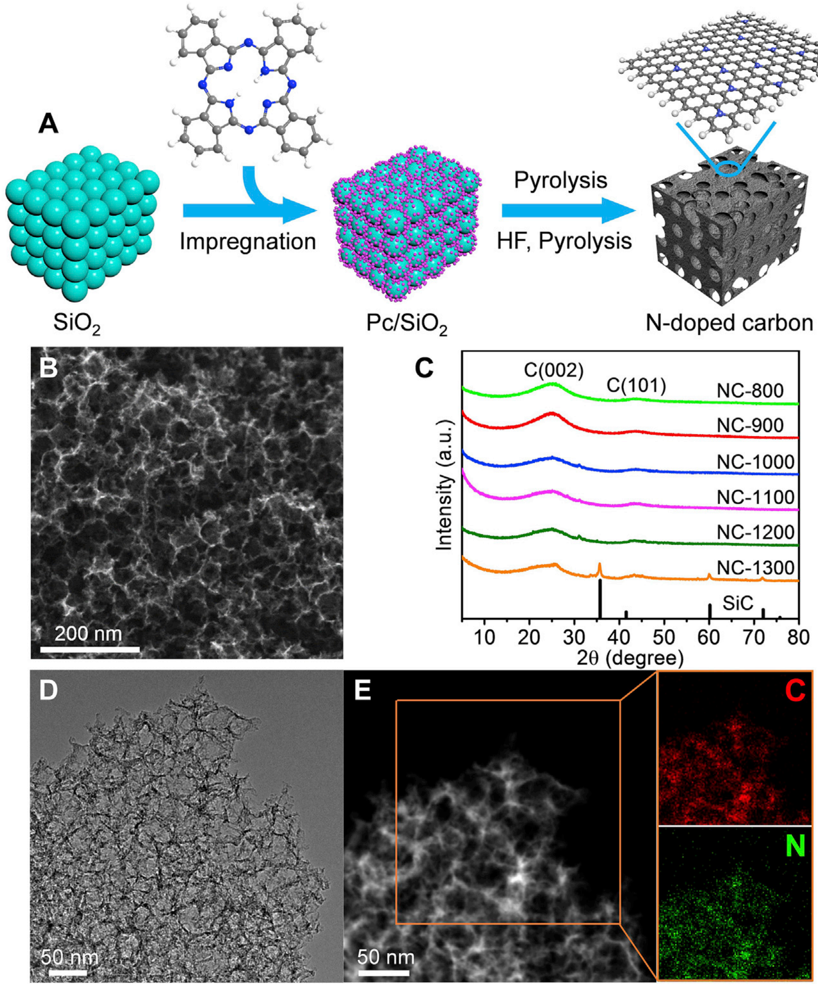

Figure 1. Schematic Synthesis Process and Structural Characterizations of N-Doped Carbon (NC) Foams

(A) Schematic illustration of the synthesis of NC foams.

(B) SEM image of the NC foam synthesized at 1,100°C (NC-1100).

(C) XRD spectra of NC foams. The small peak at 31° in the NC-1000, NC-1100, and NC-1200 samples is assigned to residual SiO_2, which is encapsulated by the C layers and has no effect on the catalytic performance.

(D) TEM image of NC-1100.

(E) HAADF-STEM image and corresponding EDX maps of the NC-1100.

can be stably maintained for 80 h. Theoretical calculations show that GN dopants can significantly enhance the electrocatalytic activity for CO_2R to CO at the adjacent C atoms, while the PN dopants promote the hydrogen evolution reaction (HER) at the adjacent C atoms, and the ProN dopants disfavors both competitive reactions.

RESULTS AND DISCUSSION

Synthesis and Characterizations of NC Foams

All of the NC foams in this study were synthesized in a template-assisted pyrolysis procedure but at different temperatures ranging from 800°C to 1,300°C to tailor the N species as shown in Figure S1. The schematic illustration of synthesis procedures is shown in Figure 1A. Phthalocyanine (Pc) was pyrolyzed with a SiO_2 nanosphere template, and the obtained NC foams were labeled NC-800, NC-900,

Please cite this article in press as: Zhang et al., Unveiling the Active Site of Metal-Free Nitrogen-doped Carbon for Electrocatalytic Carbon Dioxide Reduction, Cell Reports Physical Science (2020), https://doi.org/10.1016/j.xcrp.2020.100145

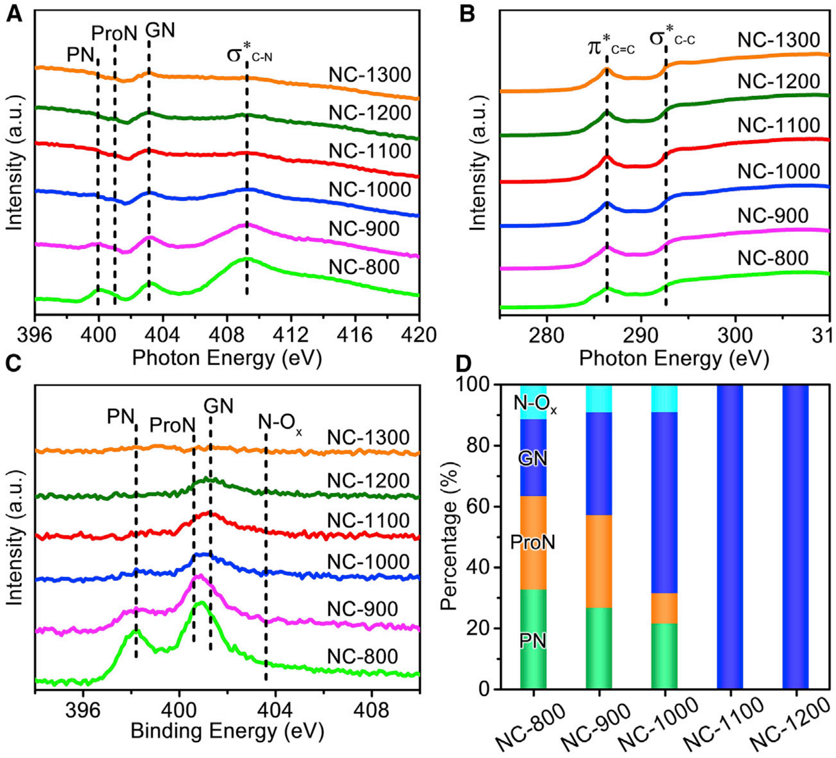

Figure 2. Variation of Electronic Structures and N Distributions in the NC Foams

(A) N K-edge NEXAFS spectra of NC foams.

(B) C K-edge NEXAFS spectra of NC foams.

(C) High-resolution N 1s XPS spectra of NC foams.

(D) The corresponding atomic percentages of different N species fitted from the XPS curves (Figure S11) of the samples.

NC-1000, NC-1100, NC-1200 and NC-1300 according to the synthetic temperature (see Experimental Procedures for more details). Scanning electron microscopy (SEM) and transmission electron microscopy (TEM) images of the as-prepared catalysts show that they possess similar porous morphology because they use the same SiO_2 nanosphere template (Figures 1B, 1D, and S2–S7), which can enhance mass transport during the CO_2R reaction. High-resolution TEM (HRTEM) analyses show that the lattice spacing of the NC foams is ~3.5 Å (Figures S2–S7), which corresponds to the (002) lattice plane of graphite C, thereby denoting that the NC is composed of graphene nanosheets.[21,22] This is further confirmed by X-ray diffraction (XRD) characterizations of all of the materials that show the typical diffraction peaks at 25.0° and 43.6°, denoting the phase of graphitic C (Figure 1C).[23,24] Raman spectra (Figure S8) also demonstrate that these materials are composed of C with a similar graphitized structure. The high angle annular dark field-scanning transmission electron microscopy (HAADF-STEM) image and corresponding elemental mappings (Figure 1E) show that N atoms are homogeneously dispersed in the C matrix.

To elucidate the electronic structure and element composition of the NC foams with increasing temperature, synchrotron-based near-edge X-ray absorption fine structure (NEXAFS) measurements for N and C were carried out on the soft X-ray beamline. The peaks at 399.9 eV, 401.0 eV, and 403.1 eV in the N K-edge NEXAFS spectra (Figure 2A) are assigned, respectively, to PN, ProN, and GN.[25–27] PN and ProN decrease significantly, and only the GN is left when the temperature increases to

1,100°C. In addition, C K-edge NEXAFS spectra (Figure 2B) show that the C species are almost unchanged for all of the samples, since they were prepared at high temperatures ranging from 800°C to 1,300°C and thereby possess good crystallinity. Survey X-ray photoelectron spectroscopy (XPS) spectra of the NC foams show that they are metal-free catalysts (Figure S9), which is further confirmed in the element analysis of NC-1100 by using inductively coupled plasma mass spectrometry (ICP-MS) (Table S1), detecting no metal signals. The high-resolution XPS of N 1s signals (Figure 2C) indicates the coexistence of four types of N species, including the PN (398.2 eV), ProN (400.6 eV), GN (401.3 eV), and N-O_x (403.6 eV) for the NC-800.[28–30] With the increase in the synthetic temperature, the relative contents (in percentage) of the PN, ProN, and N-O_x decrease significantly, while those of the GN increase (Figure 2D). When the temperature reaches 1,100°C (NC-1100), only the GN is left in the C. At 1,300°C, most N species are removed and hardly detected by the XPS. No visible change is observed in the C 1s spectra (Figure S10) of these catalysts, which is consistent with the C K-edge NEXAFS characterizations. The similarity in the chemical state of the C framework was also reflected in the Raman spectra of the NC samples, which shows that the intensity ratios of the D band to G band peaks (I_D/I_G) are ~1.01 for the samples from NC-800 to NC-1200 (Figure S8), indicating that they have similar crystallinity. The slight increase in the I_D/I_G to 1.18 from NC-1200 to NC-1300 may be due to the formation of a few C defects with the removal of N dopants, as shown in the N 1s XPS (Figure 2C).

Electrocatalytic Performance for the CO_2R

Electrochemical performance tests of these catalysts were investigated in a two-compartment H-type cell with an electrolyte of 0.5 M $KHCO_3$.[31] Gas chromatography (GC) and nuclear magnetic resonance (NMR) analyses were used to confirm that H_2 and CO are the products. For the NC-1100 sample, which is dominated by GN dopants (Figure 2D), linear sweep voltammetry (LSV) measurements show a significant increase in the current density with a potential of −0.4 V as the electrolyte was saturated by CO_2 (Figure 3A), which demonstrates that the GN dopants can induce high activity for the CO_2R to CO. To illustrate the roles of different N types in catalyzing the CO_2R to CO, the Faradaic efficiencies (FEs) of the two products (CO and H_2) were measured for all of the NC samples (Figures 3B and S12), which shows that the CO Faradaic efficiency (FE_{CO}) grows gradually as the percentage of GN increases from ~25% of NC-800 to 100% of NC-1100 (Table S2), while the FE_{H2} is lowered accordingly. The NC-1200 mainly has GN dopants in the C lattice, although with reduced content, the FE_{CO} is close to that of the NC-1100. The much-lowered FE for NC-1300 is due to the removal of most of the N dopants during the preparation process at the high temperature, thus leading to poor activity for the CO_2R to CO. The SiC in the NC-1300 sample formed by high-temperature calcination barely has an effect on the CO_2R to CO activity (Figure S13). Although the GN content and the CO_2R to CO activity of these samples is not linearly correlated, which may be affected by their microstructures, we can find an overall trend that the FE_{CO} over the NC catalysts rises with increasing GN contents.

To investigate the effect of oxygen (O) dopants on the electrocatalytic CO_2R to CO activity,[32,33] the contents of O in the NC samples were also measured by using XPS (Figure S14A). However, no clear relation was found between the trend of FE_{CO} and the content of O (Figure S14B), thus indicating that the O dopants are not likely active sites for the electrocatalytic CO_2R to CO. In addition, to determine the contribution of C defects to the CO_2R to CO activity,[34–36] the activity of pure C foam (C-1100) possessing morphology and defects similar to those of the NC samples

Please cite this article in press as: Zhang et al., Unveiling the Active Site of Metal-Free Nitrogen-doped Carbon for Electrocatalytic Carbon Dioxide Reduction, Cell Reports Physical Science (2020), https://doi.org/10.1016/j.xcrp.2020.100145

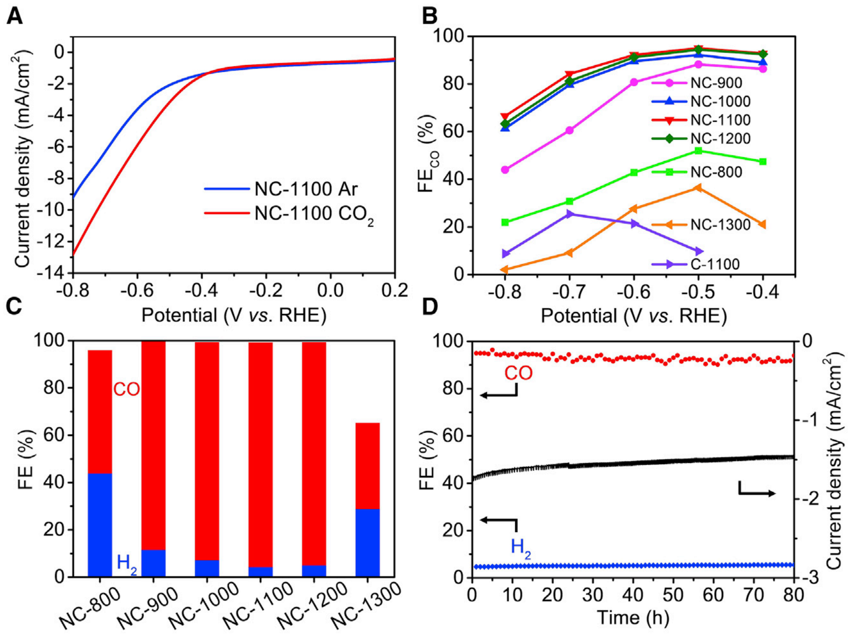

Figure 3. Electrocatalytic Performance of the NC Foams

(A) LSV curves of the NC-1100 in Ar- or CO_2-saturated electrolytes.

(B) FE_{CO} over the NC catalysts and pure C foam. The current density at −0.4 V versus RHE for the C-1100 sample is too low, so the exact Faradaic efficiencies can hardly be calculated and thus is not shown.

(C) Comparison in the FE for the formation of CO and H_2 at −0.5 V versus RHE.

(D) Stability test of the NC-1100 at −0.5 V versus RHE.

(Figures S15 and S16) was also investigated for comparison, which exhibits a significantly lower FE for the formation of CO (Figures 3B and S17), thus denoting that C defects in the NC foams are much less active than GN-doped C sites for the CO_2R to CO.

At −0.5 V versus RHE, where the highest FE_{CO} was achieved over the NC samples, the FEs of CO and H_2 were directly compared in Figure 3C. This shows that the GN-enriched NC-1100 is more selective to the CO_2R to CO, with a maximum FE_{CO} of up to 95%, while the PN-ProN-enriched NC-800 is more selective to the HER, thus revealing that the GN dopants trigger the electrocatalytic activity for the CO_2R to CO over the NC catalyst. The high FE of the NC-1100 surpasses most of the other metal-free electrocatalysts for CO_2R to CO in the $KHCO_3$ electrolyte in the previous reports (Table S3), and the high FE_{CO} can be stably maintained for 80 h at −0.5 V versus RHE (Figure 3D). The N 1s XPS spectra of NC-1100 after the stability test were also measured (Figure S18), which shows the appearance of ProN dopants and indicates that part of the GN was transformed into ProN during the reaction process. The slight decreases in the total current density and FE_{CO} during the stability test further suggest that the GN-doping is the origin of activity for the CO_2R to CO. Moreover, an isotope-labeled experiment of the electrochemical $^{13}CO_2$ reduction to CO over the NC-1100 was also conducted, in which no clear peak at *m/z* 28 was observed in the mass spectrum of products, showing no ^{12}CO was produced during the reaction process (Figure S19). This confirms that the CO is produced from the CO_2 reduction rather than from the catalyst degradation.

Please cite this article in press as: Zhang et al., Unveiling the Active Site of Metal-Free Nitrogen-doped Carbon for Electrocatalytic Carbon Dioxide Reduction, Cell Reports Physical Science (2020), https://doi.org/10.1016/j.xcrp.2020.100145

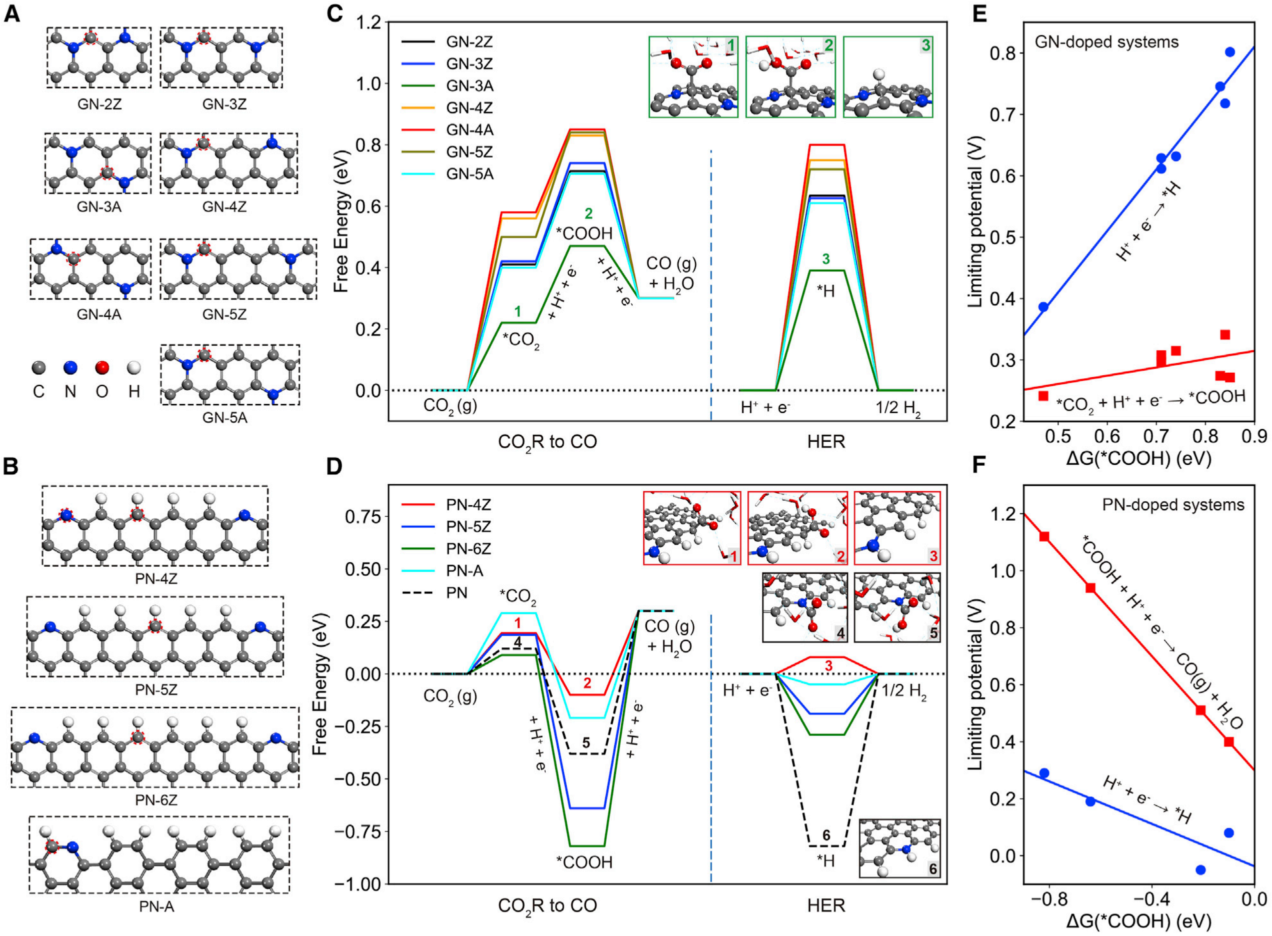

Figure 4. Theoretical Studies of the Catalytic Activities of GN and PN in the Electrochemical CO_2R to CO and the HER

(A and B) Atomic structures for the GN-doped graphene (A) and the PN-doped graphene nanoribbon models (B) (Figure S20). The red dotted circles denote the sites for studying the reaction mechanisms.

(C and D) Free energy pathways for the CO_2R to CO and the HER over the GN-induced (C) and the PN-induced (D) active sites at 0 V versus the RHE. The insets show the structures of the reaction intermediates.

(E and F) Limiting potentials for the CO_2R to CO and the HER reactions as functions of the formation free energies of *COOH (ΔG(*COOH)) over the GN-induced (E) and the PN-induced (F) active sites.

Theoretical Investigation of the Active Sites

To gain insights into the electrocatalytic activities of the catalysts induced by different N dopants, we conducted density functional theory (DFT) studies of the CO_2R to CO and the HER. Two-dimensionally (2D) periodic graphene doped with GN and 1D graphene nanoribbons doped with PN or ProN at the edges were used for modeling the catalysts (Figure S20). The effect of N-doping content was considered by using two N dopants in a supercell with varied distances between them (Figures 4A, 4B, and S21). In the GN-doped graphene, the C atoms next to the GN dopants are triggered and thus are used as the reactive sites for the reactions.[37] For the PN- and ProN-doped nanoribbons, the C atoms at the edges are investigated as the reactive sites.[38] The GN and ProN sites are inactive for the adsorption of CO_2 and H. The PN-O_x species can be readily hydrogenated to N-OH and then further reduced to PN with free energy changes of −0.21 and −1.52 eV, respectively. The adsorption of H* on the PN site being exergonic by −0.82 eV in free energy is much stronger than the adsorption of CO_2 being endergonic by 0.12 eV, which is similar to the results reported by Wu et al.[11] The strong adsorption of H* on the PN is an important factor to be considered, which implies that the PN site is prone to be poisoned by the H* and thus is not likely an active site for the CO_2R to CO.[18]

The potential for the CO_2R to CO is determined by the charge-transfer step that has the most positive free energy change. The CO_2 adsorption step does not involve the transfer of an electron but is thermally surmountable with moderate uphill reactions in free energy at the GN-, PN-, and ProN-induced active sites. In the following electron-involved steps, the endergonic $^*CO_2$ hydrogenation to *COOH is the potential-determining step for the CO_2R to CO over the GN-doped surfaces (Figure 4C), the limiting potentials of which are obviously lower than those of the HER (Figure 4E), demonstrating that the GN-induced sites are more selective for the CO_2R to CO. However, at the PN-doped graphene edge sites, the hydrogenation of *COOH to CO and H_2O becomes more endergonic and is the potential-determining step (Figure 4D), with much higher limiting potentials than those of the HER (Figure 4F); this demonstrates that the PN-induced sites are more active for the HER. At the ProN-doped edge sites, both the limiting potentials of the CO_2R to CO and the HER are quite high, which are ~0.82 and 0.58 V, respectively (Figure S21). Therefore, DFT results demonstrate that the doping of GN favors the electrochemical CO_2R to CO over the HER, while the PN-doping can induce a higher HER activity and ProN-doping is unfavorable for both the CO_2R to CO and the HER.

A mixed-phase N-doping effect on the CO_2R to CO and HER activities is also studied by using the adsorption free energy of H* ($\Delta G(H^*)$) as a descriptor based on the linear relations between the limiting potentials of the CO_2R to CO and the $\Delta G(H^*)$, which can be established based on the above results of single-phase N-doping cases (Figures S20 and S22). From the calculated $\Delta G(H^*)$ on different active sites of the mixed-phase N-doped structure, which are 0.87, −0.24, and 0.35 eV on the GN-, PN-, and ProN-doped C sites, respectively, the corresponding limiting potentials of the CO_2R to CO are 0.31, 1.00, and 0.54 eV, respectively, from the linear relations (Figure S22). Thus, we can obtain similar results that in the mixed-phase N-doped structure, the CO_2R to CO is favored on the GN-doped C site, while the HER is favored on the PN-doped site, and both are disfavored on the ProN-doped site.

The electronic density of states (DOS) of the C sites modulated by the three types of N dopants was calculated to understand their different reactivities (Figure S23). The PN-doped C site possesses high DOS near the Fermi level, leading to overly strong adsorption of COOH* on the site, and thus a high limiting potential for the hydrogenation of COOH* to CO. In comparison, the density of states on the GN-doped C site is moderately lowered near the Fermi level, which weakens the adsorption of COOH* and thus reduces the limiting potential. The ProN-doped C possesses a much lower DOS so that the adsorption of COOH* is too weak and the hydrogenation of CO_2^* to COOH* requires a high limiting potential.

In summary, NC foams with various types and contents of N have been synthesized to reveal the active sites for electrocatalytic CO_2R to CO. Electrocatalytic performance shows that GN-doped C shows significant enhancement in CO production. The optimized NC-1100 with dominated GN exhibits the highest FE_{CO}, achieving 95% at −0.5 V versus RHE, and possesses a long-term stability of 80 h. The underlying reaction mechanism has been unveiled by DFT calculations, which demonstrates that GN-induced active C atoms are more selective for CO_2R to CO against HER,

Please cite this article in press as: Zhang et al., Unveiling the Active Site of Metal-Free Nitrogen-doped Carbon for Electrocatalytic Carbon Dioxide Reduction, Cell Reports Physical Science (2020), https://doi.org/10.1016/j.xcrp.2020.100145

while the case of PN-modified C atoms is just the opposite, and doping of ProN disfavors either the CO_2R or HER. This study reveals the catalytic nature of NC and provides guidance for the design of metal-free C materials for the electrocatalytic CO_2R.

EXPERIMENTAL PROCEDURES

Resource Availability

Lead Contact

Further information and requests for resources and reagents should be directed to and will be fulfilled by the Lead Contact, Dehui Deng (dhdeng@dicp.ac.cn).

Materials Availability

This study did not generate new unique reagents.

Data and Code Availability

The authors declare that the data supporting the findings of this study are available within the article and the Supplemental Information. All other data are available from the Lead Contact upon reasonable request.

Materials

SiO_2 colloidal dispersion (30% in ethylene glycol) was acquired from Alfa Aesar. Pc and $KHCO_3$ (99.7%) were purchased from Sigma-Aldrich. Glucose and *N*,*N*-dimethylformamide (DMF) were acquired from Sinopharm Chemical Reagent. $^{13}CO_2$ (99 atom% ^{13}C) and $NaH^{13}CO_3$ (99 atom% ^{13}C) were purchased from Cambridge Isotope Laboratories. All of the chemicals were used in this study without further purification. C fiber paper (AvCarb GDS3250) was purchased from Fuel Cell Store. All aqueous solutions were prepared with Millipore water (18.2 MΩ • cm).

Synthesis

The NC foams were synthesized through a pyrolysis method. Pc 1 g and 12 g SiO_2 colloidal dispersion were first dispersed in 80 mL DMF, followed by stirring at 80°C in an oil bath pot to remove the solvent, and then dried at 80°C in a vacuum oven. After that, 1 g gained solid was placed in a crucible and heated to 800°C at a rate of 5°C min^{-1} in an Ar atmosphere and then kept at 800°C for 2 h. The pyrolyzed sample was treated with 5% hydrofluoric acid (HF) aqueous solution to remove the SiO_2 template at room temperature, washed with deionized water, and then dried at 80°C. Finally, the obtained powder was pyrolyzed at 800°C for 2 h in an Ar atmosphere to obtain the final catalyst. To modify the N types and contents, different pyrolysis temperatures (800°C, 900°C, 1,000°C, 1,100°C, 1,200°C, and 1,300°C) have been investigated with the same synthetic method. The resulting materials were denoted as NC-800, NC-900, NC-1000, NC-1100, NC-1200, and NC-1300, respectively.

For the NC-1300 sample, to rule out the effect of SiC contaminant on the CO_2R to CO activity, an alternative synthesis process was used to prepare the NC-1300 without SiC (NC-1300-pure). Pc 1 g and 12 g SiO_2 colloidal dispersion were dispersed in 80 mL DMF, stirred at 80°C in an oil bath pot to remove the solvent, and then dried at 80°C in a vacuum oven. After that, 1 g gained solid was placed in a crucible and heated to 800°C at a rate of 5°C min^{-1} in an Ar atmosphere, and then kept at 800°C for 2 h. The pyrolyzed sample was treated with 5% HF aqueous solution to remove the SiO_2 template at room temperature, washed with deionized water, and then dried at 80°C. Finally, the obtained powder was pyrolyzed at 1,300°C for 2 h in an Ar atmosphere to obtain the final catalyst.

To synthesize pure C foam, 1 g glucose and 12 g SiO_2 colloidal dispersion were dispersed in 80 mL deionized water, stirred at 80°C in an oil bath pot to remove the solvent, and then dried at 80°C in a vacuum oven. After that, 1 g gained solid was placed in a crucible and heated to 1,100°C at a rate of 5°C min^{-1} in an Ar atmosphere, and then kept at 1,100°C for 2 h. The pyrolyzed sample was treated with a 5% HF aqueous solution to remove the SiO_2 template at room temperature, washed with deionized water, and then dried at 80°C. Finally, the obtained powder was pyrolyzed at 1,100°C for 2 h in an Ar atmosphere to obtain the final catalyst, which was denoted as C-1100.

Characterization

SEM measurement was conducted on Hitachi S5500. TEM measurements were conducted on an FEI Tecnai F20 microscope operated at an accelerating voltage of 200 kV. XRD measurements were carried out on a Rigaku Ultima IV diffractometer with Cu Ka radiation (λ = 1.5418 Å) at 40 kV and 30 mA. The XRD measurement of NC-1300 without SiC was carried out on a Rigaku D/MAX 2500 diffractometer with Cu Kα radiation at a voltage of 40 kV and a current of 200 mA. Raman spectra were performed on a Jobin-Yvon Horiba Xplora confocal Raman system with a 532-nm excitation laser at a power of ~0.3 mW. ICP-MS was performed on a PerkinElmer NexION 300D. XPS measurements were carried out on the ESCALAB 250 system used Al Kα X-rays as the excitation source (1,486.68 eV). In addition, XPS measurements for NC-1100 before and after the stability test were performed on an Omicron XPS System using Al Kα X-rays as the excitation source, with a voltage of 15 kV and power of 300 W. All binding energies for XPS measurements were calibrated using C 1s peak with a binding energy of 284.6 eV. The synchrotron-based soft X-ray absorption spectra were carried out at the photoemission endstation of the BL10B beamline in the National Synchrotron Radiation Laboratory (NSRL) with the total electron yield (TEY) mode. ^{1}H NMR spectra were recorded with a Bruker 500 MHz NMR instrument.

Electrochemical Measurements

Electrochemical measurements were conducted using an electrochemical workstation (CHI760E) connected to a gas-tight H-cell with 2 chambers separated by Nafion 115 membrane. Each chamber contained 45 mL of 0.5 M $KHCO_3$. Pt net was used as a counter electrode, along with an Ag/AgCl reference electrode (saturated KCl). All potentials were measured against Ag/AgCl, which were converted to RHE. RHE was converted by the conversion formula as follows: E (versus RHE) = E (versus Ag/AgCl) + 0.1989 V + 0.059 × pH. The catalyst of ethanol solution was brushed onto the C fiber paper to form 2 mg cm^{-2} with 10% Nafion content (covering a 1 × 1-cm^2 area) as the working electrode. All of the electrochemical experiments were performed at 25°C.

LSV tests were performed in Ar-saturated (pH = 8.8) and CO_2-saturated (pH = 7.2) 0.5 M $KHCO_3$ solutions with a scan rate of 5 mV/s without stirring. The controlled potential electrolysis was performed with slight stirring to measure the FEs of the reduction products. CO_2 was purged continuously at a rate of 10 mL min^{-1} through the mass flow meter. The gas-phase products were analyzed by online GC (GC-2014) using one thermal conductivity detector (TCD) and two flame ionization detectors (FIDs), one FID for hydrocarbon compounds and the other FID equipped with a methane conversion oven for low CO concentrations. The liquid-phase product was analyzed using ^{1}H NMR. The sum of FEs for NC-1300 is far less than 100%, as the extremely low current density during the controlled potential electrolysis test, leading to an inevitably large error for the calculating results.

Please cite this article in press as: Zhang et al., Unveiling the Active Site of Metal-Free Nitrogen-doped Carbon for Electrocatalytic Carbon Dioxide Reduction, Cell Reports Physical Science (2020), https://doi.org/10.1016/j.xcrp.2020.100145

To determine the origin of product CO, an isotope-labeled experiment was carried out under the same reaction conditions by using 0.5 M $NaH^{13}CO_3$ and $^{13}CO_2$ as the feedstock. The product was analyzed by using MS of HQT-001 (Dalian Institute of Chemical Physics, Chinese Academy of Sciences).

Faradaic Efficiency

The FEs of reduction products are calculated as follows:

$$i_{H_2 \ \text{or} \ CO} = \upsilon_{H_2 \ \text{or} \ CO} \times V \times \frac{2Fp_0}{RT} \qquad \text{(Equation 1)}$$

$$FE_{H_2 \ \text{or} \ CO} = \frac{i_{H_2 \ \text{or} \ CO}}{i_{total}} \times 100\% \qquad \text{(Equation 2)}$$

where $i_{H_2 \ or \ CO}$ is the current density of H_2 or CO acquired from CHI760E, $\upsilon_{H_2 \ or \ CO}$ is the volume concentration of H_2 or CO acquired from GC-2014, V is the gas volume flow rate at room temperature and under ambient pressure, F is the Faradaic constant, p_0 is pressure, R is the ideal gas constant, T is temperature, $FE_{H_2 \ or \ CO}$ is the FE of H_2 or CO, and i_{total} is the total current density.

Computational Methods

DFT calculations were performed using the Vienna Ab-initio Simulation Package (VASP).[39–42] The projector augmented-wave pseudopotential method with the Perdew-Burke-Ernzerhof (PBE) exchange-correlation functional and a plane-wave cutoff energy of 400 eV was adopted.[43–46] The zero-damping DFT-D3 method of Grimme and associates[47,48] was used to calculate the van der Waals correction. 2D periodic graphene models doped with two N atoms at different distances were used to simulate the doping effect of graphitic N; 1D graphene nanoribbon models with a zigzag edge and an armchair edge were used to simulate the pyridinic N-doping, and those with an armchair edge were used to simulate the pyrrolic N-doping (Figure S20). The vacuum thicknesses were set larger than 15 Å between the layers. Monkhorst-Pack k-point sampling of 3 × 3 × 1 and 3 × 1 × 1 were selected for the 2D and 1D models, respectively.[49] The convergence standard for structural optimizations was set below 0.02 eV/Å for the residual forces between atoms. Dipole correction was applied to decouple the interactions between the slabs or nanoribbons.

The free energies of reaction intermediates on the surface were calculated as $E_{\text{total}} + \text{ZPE} - TS$, where E_{total} is DFT calculated total energy, ZPE is the zero-point energy, T is temperature, and S is the entropy from vibrational contribution under the harmonic oscillation approximation. The free energy of $(H^+ + e^-)$ was calculated as that of $^1/_2$ H_2. The free energy of gas molecules was calculated as E_{total} + ZPE $\int_0^T C_p dT - TS$, in which $\int_0^T C_p dT$ is the integrated heat capacity from 0 K to T. For the ZPE $\int_0^T C_p dT - TS$ parts, we used the experimental data from the National Institute of Standards and Technology (NIST) database. The formation free energy was calculated by using CO_2 and H_2 gas molecules as the reference states. In calculating the reaction mechanisms of the CO_2R to CO, a few water layers were added surrounding the reaction intermediates to simulate the water environment and the stabilization effect from the H bonding.

SUPPLEMENTAL INFORMATION

Supplemental Information can be found online at https://doi.org/10.1016/j.xcrp.2020.100145.

ACKNOWLEDGMENTS

We gratefully acknowledge the financial support of the National Key R&D Program of China (2016YFA0204100, 2016YFA0200200, and 2017YFA0403403), the National Natural Science Foundation of China (21890753, 21988101, 91845106, and U1732272), the Strategic Priority Research Program of Chinese Academy of Sciences (CAS) (XDB36030200), the Key Research Program of Frontier Sciences of the Chinese Academy of Sciences (QYZDB-SSW-JSC020), and the DNL Cooperation Fund, CAS (DNL180201).

AUTHOR CONTRIBUTIONS

D.D. conceived the project and designed the experiments. Z.Z. prepared the samples and performed the electrochemical experiments. L.Y. conducted the DFT calculations. Y.T. and R.C. assisted with the partial experiments. L.W. and J.Z. assisted with the NEXAFS measurements. Z.Z., L.Y., and D.D. analyzed the experimental data and co-wrote the manuscript.

DECLARATION OF INTERESTS

The authors declare no competing interests.

Received: January 4, 2020
Revised: June 23, 2020
Accepted: July 3, 2020
Published: August 12, 2020

REFERENCES

1. Gu, J., Hsu, C.-S., Bai, L., Chen, H.M., and Hu, X. (2019). Atomically dispersed Fe^{3+} sites catalyze efficient CO_2 electroreduction to CO. Science *364*, 1091–1094.
2. Han, N., Wang, Y., Ma, L., Wen, J., Li, J., Zheng, H., Nie, K., Wang, X., Zhao, F., Li, Y., et al. (2017). Supported cobalt polyphthalocyanine for high-performance electrocatalytic CO_2 reduction. Chem *3*, 652–664.
3. Jiang, K., Siahrostami, S., Akey, A.J., Li, Y., Lu, Z., Lattimer, J., Hu, Y., Stokes, C., Gangishetty, M., Chen, G., et al. (2017). Transition-metal single atoms in a graphene shell as active centers for highly efficient artificial photosynthesis. Chem *3*, 950–960.
4. Nielsen, D.U., Hu, X.-M., Daasbjerg, K., and Skrydstrup, T. (2018). Chemically and electrochemically catalysed conversion of CO_2 to CO with follow-up utilization to value-added chemicals. Nat. Catal. *1*, 244–254.
5. Ren, S., Joulié, D., Salvatore, D., Torbensen, K., Wang, M., Robert, M., and Berlinguette, C.P. (2019). Molecular electrocatalysts can mediate fast, selective CO_2 reduction in a flow cell. Science *365*, 367–369.
6. Varela, A.S., Ju, W., Bagger, A., Franco, P., Rossmeisl, J., and Strasser, P. (2019). Electrochemical Reduction of CO_2 on Metal-Nitrogen-Doped Carbon Catalysts. ACS Catal. *9*, 7270–7284.
7. Wang, Y., Mao, J., Meng, X., Yu, L., Deng, D., and Bao, X. (2019). Catalysis with Two-Dimensional Materials Confining Single Atoms: Concept, Design, and Applications. Chem. Rev. *119*, 1806–1854.
8. Duan, X., Xu, J., Wei, Z., Ma, J., Guo, S., Wang, S., Liu, H., and Dou, S. (2017). Metal-Free Carbon Materials for CO_2 Electrochemical Reduction. Adv. Mater. *29*, 1701784.
9. Hursán, D., and Janáky, C. (2018). Electrochemical Reduction of Carbon Dioxide on Nitrogen-Doped Carbons: Insights from Isotopic Labeling Studies. ACS Energy Lett. *3*, 722–723.
10. Hursán, D., Samu, A.A., Janovák, L., Artyushkova, K., Asset, T., Atanassov, P., and Janáky, C. (2019). Morphological Attributes Govern Carbon Dioxide Reduction on N-Doped Carbon Electrodes. Joule *3*, 1719–1733.
11. Wu, J., Liu, M., Sharma, P.P., Yadav, R.M., Ma, L., Yang, Y., Zou, X., Zhou, X.-D., Vajtai, R., Yakobson, B.I., et al. (2016). Incorporation of Nitrogen Defects for Efficient Reduction of CO_2 via Two-Electron Pathway on Three-Dimensional Graphene Foam. Nano Lett. *16*, 466–470.
12. Wu, J., Yadav, R.M., Liu, M., Sharma, P.P., Tiwary, C.S., Ma, L., Zou, X., Zhou, X.-D., Yakobson, B.I., Lou, J., and Ajayan, P.M. (2015). Achieving Highly Efficient, Selective, and Stable CO_2 Reduction on Nitrogen-Doped Carbon Nanotubes. ACS Nano *9*, 5364–5371.
13. Benzigar, M.R., Talapaneni, S.N., Joseph, S., Ramadass, K., Singh, G., Scaranto, J., Ravon, U., Al-Bahily, K., and Vinu, A. (2018). Recent advances in functionalized micro and mesoporous carbon materials: synthesis and applications. Chem. Soc. Rev. *47*, 2680–2721.
14. Dai, L., Xue, Y., Qu, L., Choi, H.-J., and Baek, J.-B. (2015). Metal-free catalysts for oxygen reduction reaction. Chem. Rev. *115*, 4823–4892.
15. Deng, D., Novoselov, K.S., Fu, Q., Zheng, N., Tian, Z., and Bao, X. (2016). Catalysis with two-dimensional materials and their heterostructures. Nat. Nanotechnol. *11*, 218–230.
16. Wood, K.N., O'Hayre, R., and Pylypenko, S. (2014). Recent progress on nitrogen/carbon structures designed for use in energy and sustainability applications. Energy Environ. Sci. *7*, 1212–1249.
17. Cui, X., Pan, Z., Zhang, L., Peng, H., and Zheng, G. (2017). Selective Etching of Nitrogen-Doped Carbon by Steam for Enhanced Electrochemical CO_2 Reduction. Adv. Energy Mater. *7*, 1701456.
18. Liu, S., Yang, H., Huang, X., Liu, L., Cai, W., Gao, J., Li, X., Zhang, T., Huang, Y., and Liu, B. (2018). Identifying Active Sites of Nitrogen-Doped Carbon Materials for the CO_2 Reduction Reaction. Adv. Funct. Mater. *28*, 1800499.
19. Sharma, P.P., Wu, J., Yadav, R.M., Liu, M., Wright, C.J., Tiwary, C.S., Yakobson, B.I., Lou, J., Ajayan, P.M., and Zhou, X.-D. (2015). Nitrogen-Doped Carbon Nanotube Arrays for High-Efficiency Electrochemical Reduction of CO_2: On the Understanding of Defects, Defect Density, and Selectivity. Angew. Chem. Int. Ed. Engl. *54*, 13701–13705.
20. Ye, L., Ying, Y., Sun, D., Zhang, Z., Fei, L., Wen, Z., Qiao, J., and Huang, H. (2020). Highly Efficient Porous Carbon Electrocatalyst with Controllable N-Species Content for Selective

Please cite this article in press as: Zhang et al., Unveiling the Active Site of Metal-Free Nitrogen-doped Carbon for Electrocatalytic Carbon Dioxide Reduction, Cell Reports Physical Science (2020), https://doi.org/10.1016/j.xcrp.2020.100145

CO_2 Reduction. Angew. Chem. Int. Ed. Engl. *59*, 3244–3251.

21. Pan, F., Li, B., Xiang, X., Wang, G., and Li, Y. (2019). Efficient CO_2 Electroreduction by Highly Dense and Active Pyridinic Nitrogen on Holey Carbon Layers with Fluorine Engineering. ACS Catal. *9*, 2124–2133.
22. Xie, J., Zhao, X., Wu, M., Li, Q., Wang, Y., and Yao, J. (2018). Metal-Free Fluorine-Doped Carbon Electrocatalyst for CO_2 Reduction Outcompeting Hydrogen Evolution. Angew. Chem. Int. Ed. Engl. *57*, 9640–9644.
23. Zhang, H., Li, J., Xi, S., Du, Y., Hai, X., Wang, J., Xu, H., Wu, G., Zhang, J., Lu, J., and Wang, J. (2019). A Graphene-Supported Single-Atom FeN_5 Catalytic Site for Efficient Electrochemical CO_2 Reduction. Angew. Chem. Int. Ed. Engl. *58*, 14871–14876.
24. Zhang, Z., Ma, C., Tu, Y., Si, R., Wei, J., Zhang, S., Wang, Z., Li, J.-F., Wang, Y., and Deng, D. (2019). Multiscale carbon foam confining single iron atoms for efficient electrocatalytic CO_2 reduction to CO. Nano Res. *12*, 2313–2317.
25. Polzonetti, G., Carravetta, V., Iucci, G., Ferri, A., Paolucci, G., Goldoni, A., Parent, P., Laffon, C., and Russo, M.V. (2004). Electronic structure of platinum complex/Zn-porphyrinato assembled macrosystems, related precursors and model molecules, as probed by X-ray absorption spectroscopy (NEXAFS): theory and experiment. Chem. Phys. *296*, 87–100.
26. Yang, H.B., Miao, J., Hung, S.-F., Chen, J., Tao, H.B., Wang, X., Zhang, L., Chen, R., Gao, J., Chen, H.M., et al. (2016). Identification of catalytic sites for oxygen reduction and oxygen evolution in N-doped graphene materials: Development of highly efficient metal-free bifunctional electrocatalyst. Sci. Adv. *2*, e1501122.
27. Zheng, Y., Jiao, Y., Zhu, Y., Li, L.H., Han, Y., Chen, Y., Du, A., Jaroniec, M., and Qiao, S.Z. (2014). Hydrogen evolution by a metal-free electrocatalyst. Nat. Commun. *5*, 3783.
28. Deng, D., Pan, X., Yu, L., Cui, Y., Jiang, Y., Qi, J., Li, W.-X., Fu, Q., Ma, X., Xue, Q., et al. (2011). Toward N-doped graphene via solvothermal synthesis. Chem. Mater. *23*, 1188–1193.
29. Lai, L., Potts, J.R., Zhan, D., Wang, L., Poh, C.K., Tang, C., Gong, H., Shen, Z., Lin, J., and Ruoff, R.S. (2012). Exploration of the active center structure of nitrogen-doped graphene-based catalysts for oxygen reduction reaction. Energy Environ. Sci. *5*, 7936–7942.
30. Wang, H., Maiyalagan, T., and Wang, X. (2012). Review on Recent Progress in Nitrogen-Doped Graphene: Synthesis, Characterization, and Its Potential Applications. ACS Catal. *2*, 781–794.
31. Zhang, Z., Xiao, J., Chen, X.-J., Yu, S., Yu, L., Si, R., Wang, Y., Wang, S., Meng, X., Wang, Y., et al. (2018). Reaction mechanisms of well-defined metal–N_4 sites in electrocatalytic CO_2 reduction. Angew. Chem. Int. Ed. Engl. *57*, 16339–16342.
32. Lu, Z., Chen, G., Siahrostami, S., Chen, Z., Liu, K., Xie, J., Liao, L., Wu, T., Lin, D., Liu, Y., et al. (2018). High-efficiency oxygen reduction to hydrogen peroxide catalysed by oxidized carbon materials. Nat. Catal. *1*, 156–162.
33. Yang, F., Ma, X., Cai, W.-B., Song, P., and Xu, W. (2019). Nature of Oxygen-Containing Groups on Carbon for High-Efficiency Electrocatalytic CO_2 Reduction Reaction. J. Am. Chem. Soc. *141*, 20451–20459.
34. Daiyan, R., Tan, X., Chen, R., Saputera, W.H., Tahini, H.A., Lovell, E., Ng, Y.H., Smith, S.C., Dai, L., Lu, X., and Amal, R. (2018). Electroreduction of CO_2 to CO on a Mesoporous Carbon Catalyst with Progressively Removed Nitrogen Moieties. ACS Energy Lett. *3*, 2292–2298.
35. Jia, Y., Zhang, L., Zhuang, L., Liu, H., Yan, X., Wang, X., Liu, J., Wang, J., Zheng, Y., Xiao, Z., et al. (2019). Identification of active sites for acidic oxygen reduction on carbon catalysts with and without nitrogen doping. Nat. Catal. *2*, 688–695.
36. Wang, W., Shang, L., Chang, G., Yan, C., Shi, R., Zhao, Y., Waterhouse, G.I.N., Yang, D., and Zhang, T. (2019). Intrinsic Carbon-Defect-Driven Electrocatalytic Reduction of Carbon Dioxide. Adv. Mater. *31*, e1808276.
37. Yu, L., Pan, X., Cao, X., Hu, P., and Bao, X. (2011). Oxygen reduction reaction mechanism on nitrogen-doped graphene: a density functional theory study. J. Catal. *282*, 183–190.
38. Deng, D., Yu, L., Pan, X., Wang, S., Chen, X., Hu, P., Sun, L., and Bao, X. (2011). Size effect of graphene on electrocatalytic activation of oxygen. Chem. Commun. (Camb.) *47*, 10016–10018.
39. Kresse, G., and Furthmüller, J. (1996). Efficient iterative schemes for ab initio total-energy calculations using a plane-wave basis set. Phys. Rev. B Condens. Matter *54*, 11169–11186.
40. Kresse, G., and Hafner, J. (1993). Ab initio molecular dynamics for liquid metals. Phys. Rev. B Condens. Matter *47*, 558–561.
41. Kresse, G., and Hafner, J. (1993). Ab initio molecular dynamics for open-shell transition metals. Phys. Rev. B Condens. Matter *48*, 13115–13118.
42. Kresse, G., and Hafner, J. (1994). Ab initio molecular-dynamics simulation of the liquid-metal-amorphous-semiconductor transition in germanium. Phys. Rev. B Condens. Matter *49*, 14251–14269.
43. Blöchl, P.E. (1994). Projector augmented-wave method. Phys. Rev. B Condens. Matter *50*, 17953–17979.
44. Kresse, G., and Joubert, D. (1999). From ultrasoft pseudopotentials to the projector augmented-wave method. Phys. Rev. B Condens. Matter Mater. Phys. *59*, 1758–1775.
45. Perdew, J.P., Burke, K., and Ernzerhof, M. (1996). Generalized Gradient Approximation Made Simple. Phys. Rev. Lett. *77*, 3865–3868.
46. Perdew, J.P., Burke, K., and Ernzerhof, M. (1996). Generalized Gradient Approximation Made Simple. Phys. Rev. Lett. *78*, 1396.
47. Grimme, S., Antony, J., Ehrlich, S., and Krieg, H. (2010). A consistent and accurate ab initio parametrization of density functional dispersion correction (DFT-D) for the 94 elements H-Pu. J. Chem. Phys. *132*, 154104.
48. Grimme, S., Ehrlich, S., and Goerigk, L. (2011). Effect of the damping function in dispersion corrected density functional theory. J. Comput. Chem. *32*, 1456–1465.
49. Monkhorst, H.J., and Pack, J.D. (1976). Special points for Brillouin-zone integrations. Phys. Rev. B *13*, 5188–5192.